iScience

CellPress
OPEN ACCESS

Article

Multimode microdimer robot for crossing tissue morphological barrier

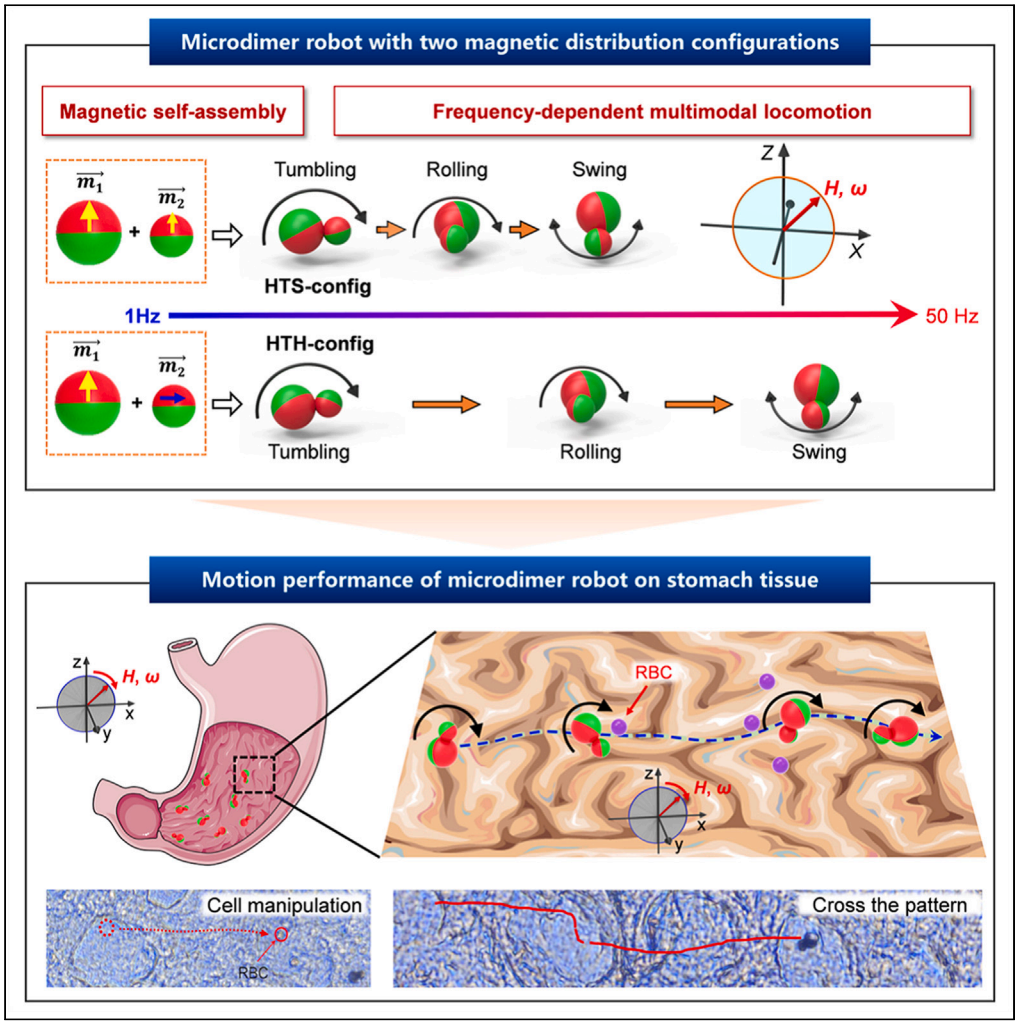

Haocheng Wang, Chenlu Liu, Xiaopeng Yang, ..., Shimin Yu, Weiwei Zhang, Tianlong Li

yushimin@ouc.edu.cn (S.Y.)
vivid@zzu.edu.cn (W.Z.)
tianlongli@hit.edu.cn (T.L.)

Highlights

Microdimer robot with two magnetic distribution configurations was fabricated

Multimodal motion of microdimer robot modulated by magnetic frequency

Magnetic dipole-dipole angle caused the dual asynchronization of microdimer robot

Crossing morphological rugae on stomach tissues by switching motion modes

Wang et al., iScience 26, 108320
November 17, 2023
https://doi.org/10.1016/j.isci.2023.108320

iScience

CellPress
OPEN ACCESS

Article

Multimode microdimer robot for crossing tissue morphological barrier

Haocheng Wang,[1,6] Chenlu Liu,[1,6] Xiaopeng Yang,[1,6] Fengtong Ji,[2,6] Wenping Song,[1,3] Guangyu Zhang,[1] Lin Wang,[1] Yanhe Zhu,[1] Shimin Yu,[4,*] Weiwei Zhang,[5,*] and Tianlong Li[1,3,7,*]

SUMMARY

Swimming microrobot energized by magnetic fields exhibits remotely propulsion and modulation in complex biological experiment with high precision. However, achieving high environment adaptability and multiple tasking capability in one configuration is still challenging. Here, we present a strategy that use oriented magnetized Janus spheres to assemble the microdimer robots with two magnetic distribution configurations of head-to-side configuration (HTS-config) and head-to-head configuration (HTH-config), achieving performance of multiple tasks through multimode transformation and locomotion. Modulating the magnetic frequency enables multimode motion transformation between tumbling, rolling, and swing motion with different velocities. The dual-asynchronization mechanisms of HTS-config and HTH-config robot dependent on magnetic dipole-dipole angle are investigated by molecular dynamic simulation. In addition, the microdimer robot can transport cell crossing morphological rugae or complete drug delivery on tissues by switching motion modes. This microdimer robot can provide versatile motion modes to address environmental variations or multitasking requirements.

INTRODUCTION

Untethered artificial microrobots have been explored to access and operate in unprecedentedly changing and hard-to-reach narrow spaces noninvasively toward precision medicine,[1,2] biotechnology,[3–6] wireless micromanipulation,[7,8] environmental remediation,[9,10] and precision detection.[11–13] In particular, magnetic microrobots driven by biocompatible magnetic fields can typically achieve robust actuation and long-range, dexterous, precise navigation.[14–17] With the trending of microrobots ranging from controllable propulsion of individuals[18,19] to the cooperative control of particle swarms,[20,21] magnetic field-driven microrobots are expected to be applied for completing tasks in biological environment.[22–24] Recent studies about magnetic micro and nanorobots mainly focus on the fabrication techniques of geometrically shaped morphology (e.g., single active particles,[25] Janus;[26] tubular;[27] flexible chain;[28,29] encoded shape-morphing[30]) and precision biomedical applications (e.g., targeted drug delivery,[31] cancer therapy,[32] minimally invasive surgery,[33] and biosensing[34]). Multipurpose and reconfigurable microrobot-based self-assembly (such as reshaped colloidal clusters,[35,36] colloidal chains,[37] supracolloidal helices;,[38] and synchronization-selected microtubes[39]) present high environmental adaptability in confined biological mediators.

"Surface walkers," as a representative of magnetical-driven microrobot, break the spatial symmetry and conduct efficient translational movement.[35,40–42] Magnetic surface walkers with frequency- and field-type-dependent multimodal motion have been developed, such as peanut colloid motors with rolling and wobbling motion modes,[43,44] and wheel-shaped flaky micro swimmers with tumbling and rolling modes.[45] When faced with inconsistent and changing biological environment, multimodal motion can provide a more effective motion mode for microrobot to adapt to the real-time environment, so as to ensure that the microrobot successfully reaches the target position and performs tasks. Such advantages provide a possibility for microrobots to perform tasks such as drug delivery and minimally invasive surgery *in vivo*. However, once the magnetic material is processed, the direction of easy magnetization under the driving magnetic field is constant, which directly determines the stable structure and movement mode of the magnetic microrobot. The stability of the properties of the magnetic components makes it difficult to realize the customization of multimodal motion of magnetic surface walker.

Inspired by the self-assembly widely existing in the natural and technological worlds (e.g., polypeptide and chiral nanomaterials), assembled aggregates open a pathway to equip magnetic surface walkers with reconfigurability and programmability.[46–49] The study from low-order microdimers[36,50,51] and microtrimers[37,38,52] to high-order microwheels[53,54] and colloidal chains[55–57] is of great importance and has

[1]State Key Laboratory of Robotics and System, Harbin Institute of Technology, Harbin, China
[2]Cancer Research UK Gurdon Institute, University of Cambridge, Cambridge, UK
[3]Chongqing Research Institute of Harbin Institute of Technology Chongqing, Chongqing, China
[4]College of Engineering, Ocean University of China, Qingdao, China
[5]School of Mechanical and Power Engineering, Zhengzhou University, Zhengzhou, China
[6]These authors contributed equally
[7]Lead contact
*Correspondence: yushimin@ouc.edu.cn (S.Y.), vivid@zzu.edu.cn (W.Z.), tianlongli@hit.edu.cn (T.L.)
https://doi.org/10.1016/j.isci.2023.108320

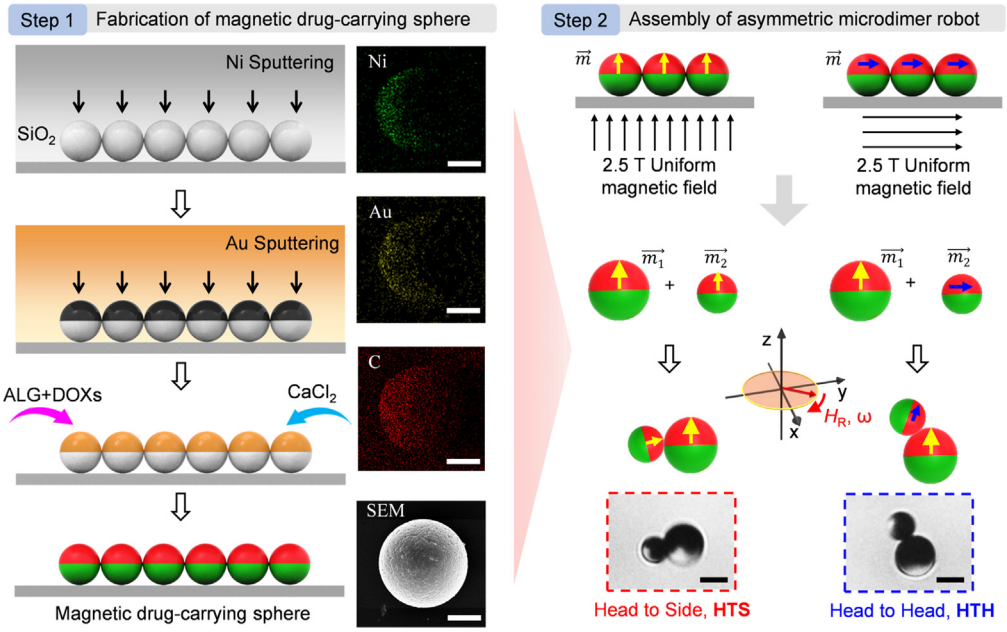

Figure 1. Magnetically triggered self-assembly and typical configurations of microdimer robot

The schematic in step 1 shows the fabrication steps of magnetic Janus particle: 90 nm of Ni layer was deposited onto a monolayer of SiO_2 microspheres to generate magnetic metallic Janus spheres. Then the Janus particles were magnetized by a 2.5 T uniform magnetic field of the horizontal or vertical direction. Two typical kinds of microdimer robots (HTS-config and HTH-config) consist of Janus microspheres with different magnetization directions and sizes self-assembled due to the magnetic dipole-dipole attraction under the rotating magnetic field (step 2). Scale bar: 2 μm.

aroused tremendous research interest. In order to customize a magnetic microrobot with modulated structure and multimode motion performance using self-assembly technology, here, we magnetized Janus microspheres at different angles to obtain magnetic Janus structure with different magnetization distributions. Furthermore, we assemble these microspheres into asymmetric multi-configuration microdimer robots with two magnetic distribution configurations of head-to-side configuration (HTS-config) and head-to-head configuration (HTH-config). The microdimer robot presented tumbling, rolling, and swing motion under rotating magnetic fields. We analyzed the multimodal motions and dual asynchronization (presenting two step-out frequencies) of microdimer robot by molecular dynamic simulation. Next, we utilized the switching of motion modes to explore the adaptive motion strategy of microdimer robot on multi topographic surfaces. Finally, the red blood cell (RBC) manipulation, topographical barriers crossing, and drug releasing on the surface of stomach using HTH-config microdimer robots were also accomplished. Comparing with the symmetric microdimer robot, the asymmetric microdimer robot with different distributions of magnetic configurations can be customized by directional magnetization of the microspheres constituting the microdimer robot, which presented different step-out frequencies and motion speeds. This microrobot with the ability of tunable multimodal motion presents high environmental adaptability and enhances task capabilities.

RESULT AND DISCUSSION

Self-assembly of multi-configuration microdimer robot

In our system, the asymmetric microdimer consists of two Janus microspheres with different sizes (5 and 8 μm) and magnetization directions to achieve self-propulsion movement mode aligning with an external magnetic field. First, magnetic drug-carrying sphere was obtained by loading doxorubicin (DOX) on the Janus microspheres deposited with nickel and gold layers through the cross-linking of sodium alginate (Step 1 in Figure 1). Elemental spectroscopy results demonstrate successful deposition of Ni and Au layers and large-area encapsulation of DOX. Then, we applied a 2.5 T uniform magnetic field parallel to and perpendicular to the deposition direction of the nickel layer to generate the different magnetization directions in Janus microspheres. A particle's dipole moment, $\vec{m}$, aligned with the field was generated. Due to the anisotropic coating, the dipole moment is shifted away from the center of the microsphere. When subjected to an external magnetic field in x-y plane, microspheres of different sizes were polarized and controlled to assemble into the asymmetric microdimer shown in Step 2 (Figure 1). The configurations of asymmetric microdimer motors assembled by microspheres with different magnetization directions were also different and controllable (Figure 1). The microdimer robot composed of two particles with same magnetization directions presents the top of 5 μm sphere's magnetic cap against the side of 8 μm sphere's magnetic cap, which is called HTS configuration. In contrast, another configuration microdimer robot called head-to-head (HTH) configuration presents the top of small particle's magnetic cap against the top of large particle's magnetic cap. The emergence of two configurations results from the interaction between the magnetic dipole moments of two microspheres and the interaction with external magnetic field. Symmetric microdimers (composed of two same spheres) and higher-order

mesostructures also generated during the self-assembly process and the motion posture of the symmetric microdimer changes continuously when the external input changes.[58] Therefore, the asymmetric basic microdimer unit was selected to explore the multimodal motion.

Multimodal motion of microdimer robot

Various monomeric[43] and swarm microrobot[44] have been reported to show multimodal motion upon changing applied magnetic field types and parameters (strength and parameters). Similar to magnetically actuated peanut motors[43] that are known to follow the rotating magnetic field with their easy-magnetization axis, our microdimer robot shows tumbling, rolling, and swinging locomotion versus the increasing input frequency (Video S1). The magnetic moments of the robots are determined by the two particles' dipole moments following their long axes for both HTH-config and HTS-config microdimer robots. When applying a rotating magnetic field, the HTH-config robot tumbled forward along long axis at low frequency. As the drive frequency increased before reaching step-out frequency, the microrobot motion gradually transitioned to rolling mode along short axis due to the increase of the fluid resistance caused by rising velocity of microdimer. With a further increase in the frequency of the magnetic field, the HTH-config microrobot gradually began to slowly step forward in a rolling mode. Figure 2A presents such switching process of multiple locomotion modes. HTS-config microrobots had the same response to the driving frequency of the magnetic field, except that the frequency corresponding mode switching is lower than that of the HTH-config microrobots. Figure 2B further details the motion decomposition of the three motion modes of tumbling, rolling, and swing. Furthermore, the trajectories of centroid of two dimer lobes with time in the three motion modes were measured and shown in Figure 2C. In our experiments, the presence of the surface wall is a key factor for microdimer swimmers to escape the constraints from the reciprocal motion for all modes of motion. In tumbling mode, the two microspheres alternatively move back and forth to drive the microdimer swimmer. Such propulsion mechanism was further revealed by tracking the trajectories of the two lobes of microdimer robot in a magnetic field at 10 mT and 2 Hz, which was different from the mode of microdimer motor at a low magnetic field strength (5 mT) in the previous study.[50]

With an increase of magnetic frequency and fluid resistance, microrobots tended to roll because of the coupling of their fluid fields and magnetic dipole forces. At this time, microdimer robot rolled along short axis and two lobes move forward in sync. Specifically, the increasing fluid resistance of the microrobot is caused by the growing speed of the microrobot as the frequency increases. However, the driving force exerted by the magnetic field is constant, so when the fluid resistance is greater than the driving force, the microrobot will change its motion posture or slip to reduce the fluid resistance. The trajectories of the two lobes at 10 mT and 22 Hz accurately reflect their synchronization of their speeds (244.25 μm/s) and the stability of rolling locomotion (Figure 2C). Further increasing the drive frequency could transform the two lobes of microdimer from a synchronous motion to an asynchronous one, which is also accompanied by the movement of the microdimer robot switching to swing mode. Such synchronization change is called step-out phenomenon which was also commonly observed for many other types of micromotors. The microdimer robot returned to the state where the two lobes alternately switch motions to drive forward. Compared with rolling mode, lobe2 still alternately moves back and forth while lobe1 moves in advance-retention (alternate forward motion and stop *in situ*) in swing mode at 10 mT and 30 Hz (Figure 2C).

To explore the mechanisms of multimodal locomotion upon changing input frequency, the flow velocities around microdimer robot at different driving frequency were simulated using the Rotating Machinery Module of COMSOL Multiphysics. Figure 2D shows the maximum velocity (80 $\mu m\ s^{-1}$) of the fluid flow at edge of the microdimer robot in a tumbling mode that is lower than one in a rolling mode (500 $\mu m\ s^{-1}$) under a simulative magnetic field of 2 and 22 Hz, respectively, suggesting a higher flow intensity in a rolling mode than that in a tumbling mode. The magnitude of the fluid flow vanishes rapidly for the microdimer robot in rolling mode as the distance from the rotation plane increases, which weakens the interaction with the surrounding fluid at high-frequency rotation. In a rolling motion mode, step-out phenomena prolonged the motion period of microdimer robot and induced a weaker surrounding flow field (Figure 2D). Note that the periodic velocity distributions with different states of the robot in tumbling and swing modes were induced by the revolution of the motor in the rotating plane, resulting in the time-varying asymmetry of the fluid flows. These simulation results indicate that the switching of various locomotion modes of the microdimer robot with increasing frequency essentially comes from the interaction between the torque generated by input magnetic field and the changing resistance caused by surrounding flow field.

Dynamics of frequency-dependent multimodal locomotion

To explore the different responses of the motion mode switching of microdimer robots with different configurations to input frequency, the effect of frequency of the rotating magnetic field on the velocity and motion mode of microdimer robot was further investigated experimentally as well. The driving frequency increased from 2 to 50 Hz with a magnetic field strength of 10 mT, as shown in Figure 3A. For the HTH-config microdimer robot of 5 + 8 μm, the velocity first went up linearly in tumbling mode as the frequency growing, reaching a maximum velocity of 98.2 μm/s. It then went down reciprocally and switch to rolling mode when the rotating magnetic field was of a "step-out" frequency of 20 Hz (ω_{c-HTH}). When the frequency further increased to 34 Hz, the motion mode changes to swing mode and keeps the speed decreasing with the increasing frequency. The velocity of HTS-config robot also shows a regular variation of first rising and then falling as frequency. Interestingly, the velocity of HTS-config robot displayed a lower peak velocity of 44.7 μm/s at a different step-out frequency of 10 Hz (ω_{c-HTS}). Similar trends in velocity and motion mode were also observed in 5 + 10 μm microdimer robot (Figure 3B). Two step-out frequency of 5 + 10 μm microdimer robot were ω_{c-HTH} = 20 Hz and ω_{c-HTS} = 14 Hz, respectively. These results suggest that the dual asynchronization of the microdimer robot resulted from the presence of two configurations is not accidental. The revelation of this mechanism can guide the magnetic configuration customization and multimode motion modulation of microdimer robots. Studies in Figure 2 have shown that the switching of motion modes of microdimer robots is the result of the combined effect of magnetic torque and hydrodynamics. As described in Figure 3A, both

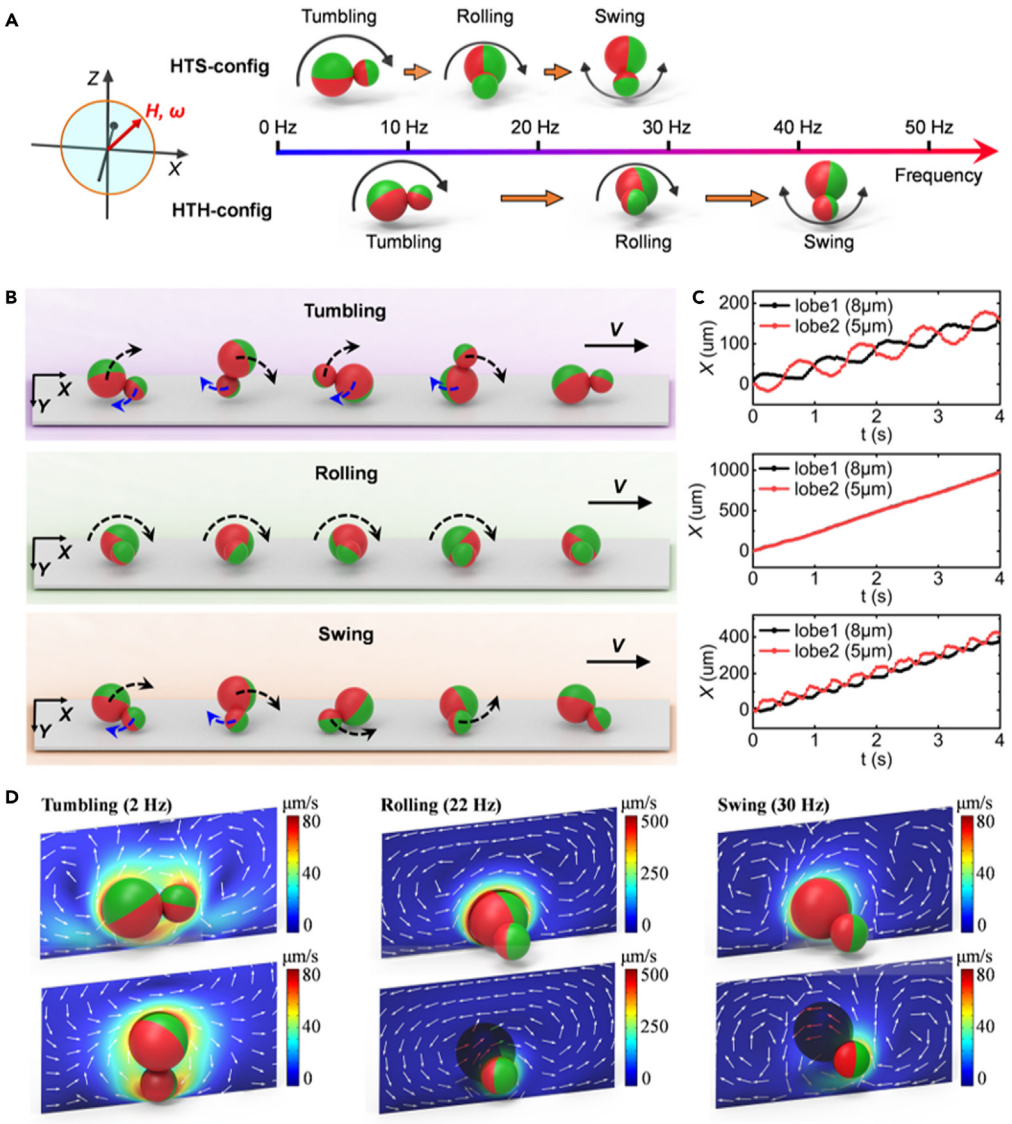

Figure 2. Frequency-dependent multimodal locomotion of microdimer robot

(A) Switching of locomotion modes of HTS-config and HTH-config microdimer robots with increasing frequency.

(B) The motion decomposition of the three motion modes of tumbling, rolling, and swing.

(C) Experimental measurement of displacement of centroid of two dimer lobes with time in tumbling, rolling, and swing modes.

(D) Flow velocities around microdimer robot at different driving frequencies.

The environmental details of experiments and simulation are shown in Table 1.

HTH-config and HTS-config microdimer robots moved in a rolling mode with similar velocities before the step-out frequency of HTS-config, suggesting they suffered a similar amount of fluid resistance. Therefore, the dual-asynchronization phenomenon mainly comes from the different magnetic torques induced by the external magnetic field in the two configurations.

Next, we analyze the equilibrium system based on the coupling of magnetic torque and hydrodynamic flow. The magnetic torque of microdimer robot mainly comes from the alignment of magnetic dipole moments and external magnetic field. The magnetic moments of the two microspheres are not aligned in the same direction after aggregating into microdimer. As a result, the magnetic moment of the microdimer is not a simple sum of the individual magnetic moments but is directly related to the distribution of the magnetic moments of the two microspheres. The magnetic dipole-dipole angles can effectively reflect the distribution of their magnetic moments and provide support for the calculation of the magnetic moment of microdimer.[59] To quantify magnetic dipole moments distribution of microdimer robots, we measured the magnetic dipole-dipole angles of 30 randomly self-assembled HTH-config and HTS-config microdimer robots actuated by a rotating magnetic field of 10 mT and 1 Hz, respectively, and presented the results in the Figure 3C. The magnetic dipole-dipole angle is defined

Table 1. Environmental details of experiments and simulation

	Selective configuration	Surface substrate	Environmental fluid	Viscosity (mpa·s)
Study on motion velocity and motion mode (Figures 2 and 3)	HTH-config HTS-config	Glass slide	DI water	1.0
Simulation of motion behavior (Figures 2 and 3)	HTH-config HTS-config	Glass slide	DI water	1.0
Translation on tissue-like topographic surfaces (Figure 4)	HTH-config	Su-8 photoresist	DI water	1.0
Locomotion in a stomach *ex vivo* (Figure 5)	HTH-config	Isolated gastric tissue mucosa	Gastric juice	1.2

Related to STAR Methods.

as the relative angle of magnetization directions of two Janus particles in microdimer robots. As can be seen, the dipole-dipole angles (θ_1) of HTS-config microdimer robots were obviously higher than those of HTH-config (θ_2), and such relationship still maintained in the larger microdimer robots. For instance, the dipole-dipole angles of HTS-config and HTH-config microdimer robot of 5 + 8 μm were $\theta_1 = 75.86°$ and $\theta_2 = 21.14°$, respectively. Similarly, the θ_1 and θ_2 of 5 + 10 μm microdimer robot were 63.58° and 30.05°, respectively, considering the HTS-config microdimer robot presented smaller step-out frequencies, which depend on the interaction of magnetic torque and fluid resistance.

To further verify whether the step-out frequency is inversely related to dipole-dipole angle, we theoretically investigated the relationship between the step-out frequency, dipole-dipole angle, magnetic torque, and fluid resistance of the HTH-config and HTS-config microdimer robots. Under the conditions of low Reynolds number ($Re < 10^{-5}$) in our experiments, the inertia can be ignored. Furthermore, the extra weight due to the coating and thermal noise was also not included in the derivation. By balancing the magnetic torque τ_m against viscous drag τ_v at the step-out frequency, we have

$$0 = \tau_v + \tau_m = -\xi_r \omega_c + \mu_w V_{Ni} \vec{m} \times \vec{H} \quad \text{(Equation 1)}$$

where ξ_r is the effective rotational friction coefficient of microdimer in the fluid,[60] ω_c is the step-out frequency, μ_w is the permeability of water, V_{Ni} is the volume of nickel coated on one particle, $\vec{m}$ is the dipole moment, and $\vec{H}$ is the external magnetic field. We solved the Equation 1 to obtain the step-out frequency $\omega_c = \mu_w V_{Ni} \vec{m} \times \vec{H} / \xi_r$. All parameters except $\vec{m}$ are the same for both HTH-config and HTS-config microdimer robots moving in tumbling mode. It is worth noting that the two configurations of the microdimer are only different in magnetic configuration and the same in structural shape, so the effective rotational friction coefficients (ξ_r) of the two are also the same. Therefore, the step-out frequencies of the two configurations have the following relationship

$$\frac{\omega_{c\text{-HTH}}}{\omega_{c\text{-HTS}}} = \frac{\overline{m}_{\text{HTH}}}{\overline{m}_{\text{HTS}}} \quad \text{(Equation 2)}$$

where $\omega_{c-\text{HTH}}$ and $\omega_{c-\text{HTS}}$ are step-out frequencies of HTH-config and HTS-config microdimer robots, respectively. $\overline{m}_{\text{HTH}}$ and $\overline{m}_{\text{HTS}}$ are the dipole moments of HTH-config and HTS-config microdimer robots, respectively. For the microdimer robot consisting two magnetic Janus microspheres, the geometric average moments can be written as

$$\overline{m}_{\text{HTH}} = \sqrt{\overrightarrow{m_1} \cdot \overrightarrow{m_2}} = \sqrt{|\overrightarrow{m_1}||\overrightarrow{m_2}| cos\,\theta_1}$$

$$\overline{m}_{\text{HTS}} = \sqrt{\overrightarrow{m_1} \cdot \overrightarrow{m_2}} = \sqrt{|\overrightarrow{m_1}||\overrightarrow{m_2}| cos\theta_2} \quad \text{(Equation 3)}$$

Where $\overrightarrow{m_1}$ and $\overrightarrow{m_2}$ are dipole moments of two microspheres that composed the microdimer. Bringing the θ_1 and θ_2 of the HTS-config and HTH-config microdimer into Equation 3 can obtain the ratio of the magnetic moments of the microdimers of the two configurations $\frac{\overline{m}_{\text{HTH}}}{\overline{m}_{\text{HTS}}} = \sqrt{\frac{0.926}{0.244}} = 1.95$, which is approximately equal to the ratio of the two step-out frequencies of the two configurations $\frac{\omega_{c\text{-HTH}}}{\omega_{c\text{-HTS}}} = \frac{20}{10} = 2$. Similarly, we also compared the ratio of magnetic moments and step-out frequencies for the two configurations of the 5 + 10 μm microdimer and observed the same results (Figure 3D). These results reveal that the difference in the angle between the magnetic moments of two spheres in two configurations causes the dual-asynchronization phenomenon.

Simulation results demonstrate that the dipole-dipole angle of HTH-config microdimer robot could weakly respond to the external load fluctuations as shown in Figure S1A. As the external load gradually stabilizes, the curve exhibits periodic fluctuations, which may be explained by the asymmetric hydrodynamic resistance caused by wall effects. Compared with HTH-config microdimer, the dipole-dipole angle fluctuation of HTS-config microdimer robot is significantly enhanced as shown in Figure S1B. This indicates that the θ_2 has a relatively strong response to load fluctuations, and the configuration stability of HTS-config microdimer robot is weak. Furthermore, the significant fluctuation of θ_2 at 0 s also reflects the possibility of significant deformation of HTS-config microdimer with sudden variation of environmental resistance.

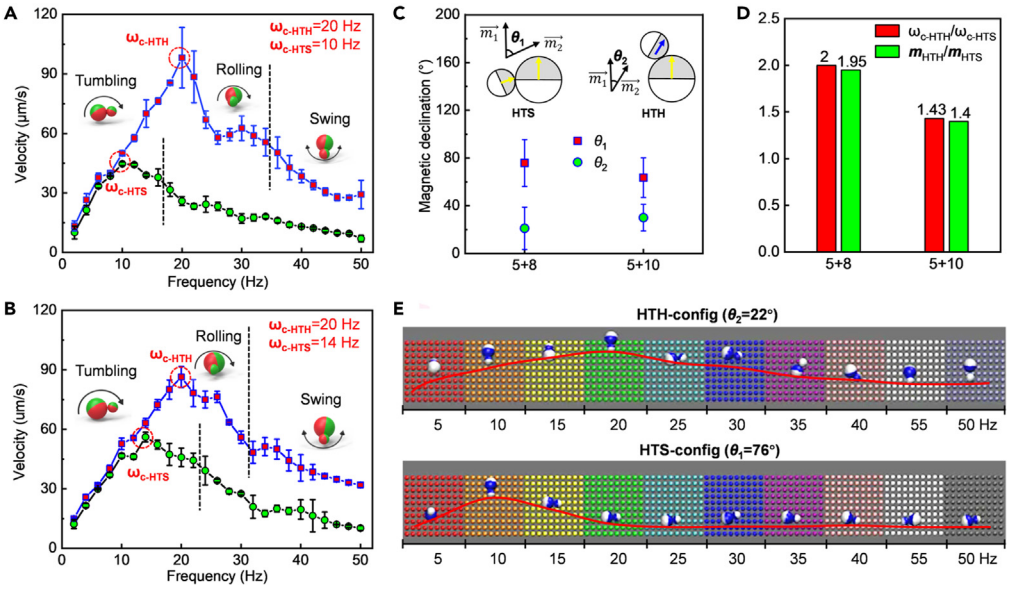

Figure 3. Frequency-dependent multimode locomotion of microdimer robot

(A and B) Average velocity versus the driving frequency of HTS-config and HTH-config microdimer robots of (A) 5 + 8 μm and (B) 5 + 10 μm. The dashed lines represent the corresponding frequency when motion modes switched.

(C) The magnetic dipole-dipole angle of HTS-config and HTH-config microdimer robots of 5 + 8 μm and 5 + 10 μm.

(D) The ratio of magnetic moments and step-out frequencies for the two configurations of the 5 + 8 μm and 5 + 10 μm microdimer robot.

(E) Molecular dynamic simulation of HTS-config and HTH-config microdimer robots of 5 + 8 μm under rotating magnetic fields with frequency from 0 to 50 Hz. Background colors represent different magnetic field frequency regions in the simulation. Representative frequencies were selected every 5 Hz from 5 to 50 Hz for motion simulation analysis during simulation operation.

The environmental details of experiments and simulation are shown in Table 1.

Molecular dynamic models of HTH-config and HTS-config microdimer robots of 5 + 8 μm were developed to further explore their dual asynchronization upon rising frequency. The quantitative parameters information of molecular dynamic simulation details was described in Part 1 of supporting information. The Janus particles were modeled as paramagnetic spheres with anisotropic magnetic susceptibility. Among the spontaneously assembled microdimers, the microdimers with $\theta_1 = 76°$ and $\theta_2 = 22°$ were selected to explore the locomotion behaviors of HTS-config and HTH-config, respectively. When applied rotating magnetic field with a magnetic field strength of 10 mT and frequency from 5 to 50 Hz, microdimer robot moved forward on the substrate surface at different velocities under different driving frequency (Video S2). By observing the relative angle between the long axis of the microdimer and its direction of motion in Figure 3E taken from Video S2, it is found that the HTH-config microdimer robot switches to rolling mode and swing mode after the frequency is increased to 15 and 25 Hz, respectively. As for the HTS-config microdimer robot, the transition of motion mode occurred when the driving frequency reached 20 and 30 Hz. The simulation results were well matched with the experimental results in Figures 3A and 3B.

During the motion, microdimer robots are subject to the fluid resistance, which may affect the stability of the magnetic configuration of microrobots. Therefore, the changes in the dipole-dipole angles during the movement of microdimer robot were simulated and analyzed. The results in Part 2 of supporting information indicated that the dipole-dipole angles (θ_1 and θ_2) of the microrobot fluctuated during its movement but remained stable overall.

Efficient translation of microdimer robot on tissue-like surfaces

For targeted medical applications at deep regions inside the human body (such as intestines, stomach etc.), heterogeneous surface topography of biological tissue rugae poses a crucial barrier for surface locomotion. Therefore, the efficient propulsion on biological surface topography of the endothelium due to organization of the endothelial cells is crucial for the microdimer robot. To preliminarily test the microdimer propulsion of different modes in *ex vivo* conditions, we fabricated vessel-like topographies, with structure heights around one to twice the size of individual endothelial cells (~4 μm) and array of slopes spaced 10 and 30 μm in X direction (Figures 4A–4C). We explored the behaviors of tumbling (5 Hz) and rolling modes (20 Hz) on different surfaces separately. Figures 4A–4C schematically present the locomotion performances of HTH-config microdimer robot tumbling and rolling on roads i, ii, and iii, respectively. It is obvious that the velocity of the two modes is not only affected by the magnetic field parameters, but also dependent on surface topographies. The motion trajectory of HTH-config microdimer robot of 5 + 8 μm in tumbling and rolling modes further illustrates the effect of surface topography on velocity (Figures 4D–4F and Video S3). On the surface i (d = 30 μm, h = 4 μm, γ = 7.5), the rolling microdimer moved faster than the tumbling one. Figure 4G shows that the velocity of tumbling and rolling microdimer on surface i was 19 and 31 μm/s, respectively. The velocity of robot in tumbling and rolling modes

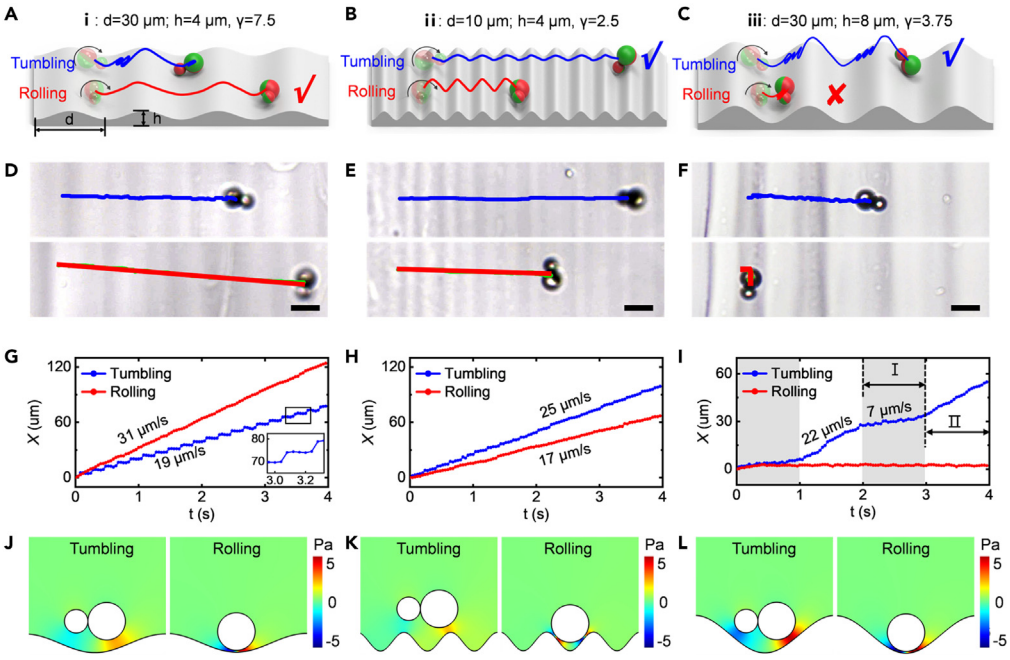

Figure 4. Microdimer robot translation on tissue-like topographic surfaces with repeating catenary features

(A–L) Microdimer robots move in tumbling and rolling modes on the topographic surfaces with aspect ratios of (A) γ = 7.5, (B) γ = 2.5, and (C) γ = 3.75, respectively. d and h respectively represent the width and height of a unit in the periodic topographic, and γ is the aspect ratio (γ = d/h). Trajectory of microdimer robots in tumbling and rolling modes in 4 s on the topographic surfaces of (D) γ = 7.5, (E) γ = 2.5, and (F) γ = 3.75, respectively. Scale bars: 10 μm. Displacement of the barycenter of microdimer robots in tumbling and rolling modes in 4 s on the topographic surfaces of (G) γ = 7.5, (H) γ = 2.5, and (I) γ = 3.75, respectively. Pressure generated around the microdimer robots in tumbling and rolling modes on the topographic surfaces of (J) γ = 7.5, (K) γ = 2.5, and (L) γ = 3.75, respectively.

The environmental details of experiments and simulation are shown in Table 1.

on topographic surfaces was lower than that on the flat surface. Notably, the rolling motion was continuous and the tumbling motion is pulsed, because of the gravitational force caused by the slope offset by the propulsion force. When microdimers were moving on surface ii with a narrower slope (d = 10 μm, h = 4 μm, γ = 2.5), the velocity of tumbling motion increased to 25 μm/s while the velocity of rolling motion decreased to 17 μm/s (Figure 4H). This is because the spacings between slopes on surface ii were similar to the body length of robot in tumbling, which effectively reduced the slip phenomenon between robot and surface. On the contrary, such array of slopes impeded the rolling motion and induced a decrease of velocity. In addition to spacings between slopes, the height of slope is another feature that reflects the topography, as described on surface iii (d = 30 μm, h = 8 μm, γ = 3.75) in Figure 4I. Although the microdimer robot can still cross the obstacle slope on surface iii using tumbling motion, it demonstrated substantial slip because the robot-slope hydrodynamic interaction weakly contributes to the net translation with the robot going uphill, which induced a higher velocity during going uphill than that during downhill. In the rolling mode, however, the climbing force generated by alternating friction was difficult for the microdimer robot to overcome gravity to climb over the slope. These results demonstrate that rolling mode processes a motion advantage on relatively flat topography, while tumbling mode is more efficient for locomotion on bumpy surfaces.

In the environment full of obstacles, the microdimer robot could break axis shifts from the underneath wall to the topography boundary, which enables the robot locomotion on the topography. However, depending on the motion mode of microdimer robot and design of the surface, the resistive forces can hinder microdimer robot locomotion near the topographies. For instance, microdimer robot cannot cross the slope on surface iii in rolling mode. In order to assess the resistive forces caused by the nearby slope, we performed 3D computational fluid dynamics analyses in which the microdimer robot with fixed positions on surface i–iii rotated in tumbling and rolling modes. For a concise comparison, we modeled the topographies structure as a 3D sinusoidal surface with different periods and amplitudes. Tumbling and rolling motion of the microdimer robot caused a fluidic pressure near the topography as shown in Figure 4J–L. For microdimer robots in the tumbling mode on different surfaces, the fluid resistance acting on the robot was inversely related to its velocity. As for the microdimer robot in rolling motion, the smaller the gap between slopes and the higher height of slope will increase the fluid resistance acting on the microdimer robot.

To investigate the ability of microdimer robot to cross higher obstacles, we further conducted on the performance of HTH-config microrobots for overcoming 20-μm-high obstacles and crossing ravines. As shown in Figure S2, initially, the microrobots approach the step with rolling motion (20 Hz) and swing motion (30 Hz), respectively. However, they encounter a barrier when they reach the step and cannot proceed. At this point, the motion mode is adjusted to rolling mode by reducing the magnetic field frequency to 5 Hz, allowing the microrobots to quickly climb over the step and continue moving forward on the flat surface. Similarly, gap can also hinder the movement of microrobots. The

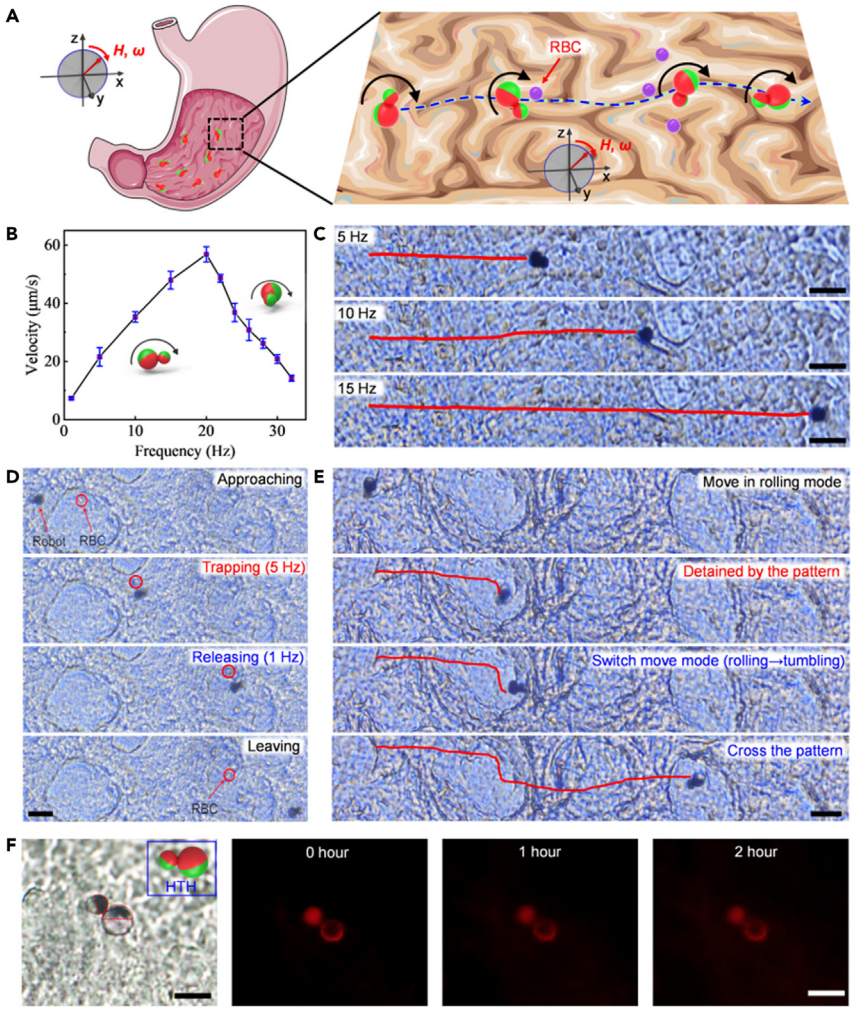

Figure 5. Cell manipulation using microdimer robots on a stomach *ex vivo*

(A) Schematic navigation and control of microdimer robots on a stomach surface.

(B) Velocity of microdimer robot on the stomach surface versus the driving frequency.

(C) Trajectory of microdimer robots in 5 s on the stomach surface under driving frequency of 5, 10, and 15 Hz, respectively. Scale bars: 20 μm.

(D) The process that a microdimer robot approached, trapped, transported, and released an RBC on the stomach surface. Scale bar: 20 μm.

(E) A microdimer robot crossing the rugaes of a stomach by switching the motion modes. Scale bar: 20 μm.

(F) Representative fluorescence images of microdimer robot during drug releasing in 2 h. Scale bar: 10 μm.

The environmental details of experiments and simulation are shown in Table 1.

microrobot self-locks when it falls down the steps in rolling mode. It can break the self-locking and continue moving forward by switching to tumbling and swing motions (Figure S3).

Ex vivo cell manipulation using microdimer robot

Efficient propulsion of HTH-config microdimer robot on surface mimicking biological surface topography opens a pathway toward application in human body. Herein, we further investigated the navigation of HTH-config microdimer robots on a stomach *ex vivo* (Figure 5A). Under the rotating magnetic field, multimode switching of the microdimer robot and cell delivery can be achieved by adjusting the driving frequency. First, we explore the change of microdimer robot's velocity with frequency on the stomach surface and the result is shown in Figure 5B. The robot tumbled forward and its velocity increased with increasing frequency until 20 Hz. Subsequently, the robot switched to rolling forward and its velocity decreased with the increasing frequency. Compared to the motion on a flat surface, the step-out frequency of the robot was similar but the overall velocity reduced by ~45%. Figure 5C further presents the trajectories of microdimer robot at different driving frequency in 5 s.

Furthermore, microdimer robot can manipulate RBC without in-depth contact through fluidic mediation in a label-free mode. A locally agitated fluidic trapping region was induced by the tumbling motion of the microdimer robot. The time-lapse images in Figure 5D, which

were captured from Video S4, present the entire process that the microdimer robot approached, trapped, transported, and released an RBC by adjusting the frequency of the rotating magnetic field. An RBC was first trapped using the locally agitated fluid induced by the tumbling motion of microdimer robot. It can then be transported at a velocity of approximately 33.6 μm/s under a rotating magnetic field of 10 mT and 5 Hz. The RBC can then be released by adjusting the frequency of the magnetic field from 5 to 1 Hz. In addition, larger topographical barriers on the surface of stomach are considerable factors hindering the locomotion of the microdimer robot. We further investigate the motility of crossing the morphological barriers on the surface of stomach by switching motion modes. As described in Figure 5E and Video S5, microdimer robot first moved rapidly in the rolling mode (20 Hz) on the surface of stomach, and then was blocked as it reached a high obstacle. Then, the motion of the microdimer robot was modulated from rolling to tumbling by decreasing the frequency to 5 Hz, which enabled the robot to climb up the morphological barrier by accumulating friction alternately and moving forward consequently. Finally, we explored the drug-releasing performance of the microdimer robot. Near-infrared irradiation (0.5 W/cm^2) was executed on microdimer robot retained on the surface of tissue and investigated the drug releasing using fluorescence microscopy. As described in Figure 5F, the increasing intensity of red fluorescence surrounding microdimer robot demonstrated the sustained drug release of microdimer robot in 2 h.

Conclusion

In conclusion, we have designed a system of multi-configuration microdimer robot self-assembled from Janus particle with different magnetization directions. The HTS-config and HTH-config microdimer robots were achieved by applying a rotating magnetic field parallel to the xoy plane. Such microdimer robots presented tumbling, rolling, and swing locomotion versus the actuation frequency. Experiments and molecular dynamics simulations were utilized to analyze the dynamic mechanism of multimodal behaviors and dual asynchronization. We found that the dual asynchronization of microdimer robots in HTS-config and HTH-config is resulted from the difference in the angle between the magnetic moments of two spheres in two configurations. The propulsion of HTH-config microdimer robot on multi topographic surfaces was also investigated to provide support for the motion control strategies of microdimer robot in changing environments. Finally, the HTH-config microdimer robots were also used to on-demand manipulating RBC and crossing larger topographical barriers on the surface of a stomach *ex vivo*. Our findings will stimulate the development of strategies to tailor the versatile assembly and functional biomedical application of actuators formed by magnetic assemblies.

Limitations of the study

The current study focused on the multimodal behavior control method of microdimer robots. Therefore, the experiments were conducted on isolated tissues *in vitro*. Future research will focus on microdimer robots performing complex tasks *in vivo*.

STAR★METHODS

Detailed methods are provided in the online version of this paper and include the following:

- KEY RESOURCES TABLE
- RESOURCE AVAILABILITY
  - Lead contact
  - Materials availability
  - Data and code availability
- METHOD DETAILS
  - Fabrication of the magnetic drug-carrying sphere
  - Magnetic actuation system
  - Environmental details of experiments
  - Simulation analysis
- QUANTIFICATION AND STATISTICAL ANALYSIS

SUPPLEMENTAL INFORMATION

Supplemental information can be found online at https://doi.org/10.1016/j.isci.2023.108320.

ACKNOWLEDGMENTS

This work was supported by the the National Key Research and Development Program (2022YFB4701700), National Excellent Youth Science Fund Project of National Natural Science Foundation of China (grant no. 52322502), the National Outstanding Youth Science Fund Project of National Natural Science Foundation of China (grant no. 52025054), China Postdoctoral Science Foundation Grant (2023M733341), National Key Research and Development Program (2022YFB4701700), the National Nature Science Foundation of China (grant no. 52175009), Heilongjiang Providence Nature Science Foundation of China (grant no. YQ2022E022), Interdisciplinary Research Foundation of HIT (IR20211219), and Fundamental Research Funds for the Central Universities.

AUTHOR CONTRIBUTIONS

H.W.: writing – original draft; C.L.: formal analysis; X.Y.: data curation; F.J.: revision; W.S.: methodology; G.Z.: resources; L.W.: investigation; S.Y.: investigation and writing – review and editing; W.Z.: software; T.L.: revision and funding acquisition.

DECLARATION OF INTERESTS

The authors declare no competing interests.

Received: June 12, 2023
Revised: August 3, 2023
Accepted: October 20, 2023
Published: October 28, 2023

REFERENCES

1. Wang, J., and Gao, W. (2012). Nano/Microscale motors: Biomedical opportunities and challenges. ACS Nano *6*, 5745–5751. https://doi.org/10.1021/nn3028997.
2. Hortelao, A.C., Simó, C., Guix, M., Guallar-Garrido, S., Julián, E., Vilela, D., Rejc, L., Ramos-Cabrer, P., Cossío, U., Gómez-Vallejo, V., et al. (2021). Swarming behavior and in vivo monitoring of enzymatic nanomotors within the bladder. Sci. Robot. *6*, eabd2823. https://doi.org/10.1126/scirobotics.abd2823.
3. Xu, T., Soto, F., Gao, W., Dong, R., Garcia-Gradilla, V., Magaña, E., Zhang, X., and Wang, J. (2015). Reversible swarming and separation of self-propelled chemically powered nanomotors under acoustic fields. J. Am. Chem. Soc. *137*, 2163–2166. https://doi.org/10.1021/ja511012v.
4. Alapan, Y., Yigit, B., Beker, O., Demirörs, A.F., and Sitti, M. (2019). Shape-encoded dynamic assembly of mobile micromachines. Nat. Mater. *18*, 1244–1251. https://doi.org/10.1038/s41563-019-0407-3.
5. Zhang, J., Mou, F., Tang, S., Kauffman, J.E., Sen, A., and Guan, J. (2022). Photochemical micromotor of eccentric core in isotropic hollow shell exhibiting multimodal motion behavior. Appl. Mater. Today *26*, 101371. https://doi.org/10.1016/j.apmt.2022.101371.
6. Li, T., Yu, S., Sun, B., Li, Y., Wang, X., Pan, Y., Song, C., Ren, Y., Zhang, Z., Grattan, K.T.V., et al. (2023). Bioinspired claw-engaged and biolubricated swimming microrobots creating active retention in blood vessels. Sci. Adv. *9*, eadg4501. https://doi.org/10.1126/sciadv.adg4501.
7. Ren, L., Nama, N., McNeill, J.M., Soto, F., Yan, Z., Liu, W., Wang, W., Wang, J., and Mallouk, T.E. (2019). 3D steerable, acoustically powered microswimmers for single-particle manipulation. Sci. Adv. *5*, eaax3084. https://doi.org/10.1126/sciadv.aax3084.
8. Zhu, H., Xu, B., Wang, Y., Pan, X., Qu, Z., and Mei, Y. (2021). Self-powered locomotion of a hydrogel water strider. Sci. Robot. *6*, eabe7925. https://doi.org/10.1126/scirobotics.abe7925.
9. Jurado-Sánchez, B., Sattayasamitsathit, S., Gao, W., Santos, L., Fedorak, Y., Singh, V.V., Orozco, J., Galarnyk, M., and Wang, J. (2015). Self-propelled activated carbon janus micromotors for efficient water purification. Small *11*, 499–506. https://doi.org/10.1002/smll.201402215.
10. Wang, H., Khezri, B., and Pumera, M. (2016). Catalytic DNA-functionalized self-propelled micromachines for environmental remediation. Chem *1*, 473–481. https://doi.org/10.1016/j.chempr.2016.08.009.
11. Huang, Y., Xu, T., Luo, Y., Liu, C., Gao, X., Cheng, Z., Wen, Y., and Zhang, X. (2021). Ultra-trace protein detection by integrating lateral flow biosensor with ultrasound enrichment. Anal. Chem. *93*, 2996–3001. https://doi.org/10.1021/acs.analchem.0c05032.
12. Feng, Y., Yuan, Y., Wan, J., Yang, C., Hao, X., Gao, Z., Luo, M., and Guan, J. (2021). Self-adaptive enzyme-powered micromotors with switchable propulsion mechanism and motion directionality. Appl. Phys. Rev. *8*, 011406. https://doi.org/10.1063/5.0029060.
13. Zheng, S., Wang, Y., Pan, S., Ma, E., Jin, S., Jiao, M., Wang, W., Li, J., Xu, K., and Wang, H. (2021). Biocompatible nanomotors as active diagnostic imaging agents for enhanced magnetic resonance imaging of tumor tissues in vivo. Adv. Funct. Mater. *31*, 2100936. https://doi.org/10.1002/adfm.202100936.
14. Wang, B., Chan, K.F., Yuan, K., Wang, Q., Xia, X., Yang, L., Ko, H., Wang, Y.X.J., Sung, J.J.Y., Chiu, P.W.Y., and Zhang, L. (2021). Endoscopy-assisted magnetic navigation of biohybrid soft microrobots with rapid endoluminal delivery and imaging. Sci. Robot. *6*, eabd2813. https://doi.org/10.1126/scirobotics.abd2813.
15. Li, J., Li, T., Xu, T., Kiristi, M., Liu, W., Wu, Z., and Wang, J. (2015). Magneto–acoustic hybrid nanomotor. Nano Lett. *15*, 4814–4821. https://doi.org/10.1021/acs.nanolett.5b01945.
16. Wu, X., Zhang, S., Lai, J., Lu, H., Sun, Y., and Guan, W. (2020). 3-D path following of helical microswimmers with an adaptive orientation compensation model. Exp. Clin. Transplant. *18*, 823–831. https://doi.org/10.1109/TASE.2019.2947071.
17. Xu, T., Gao, W., Xu, L.P., Zhang, X., and Wang, S. (2017). Fuel-free synthetic micro-/nanomachines. Adv. Mater. *29*, 1603250. https://doi.org/10.1002/adma.201603250.
18. Mou, F., Chen, C., Ma, H., Yin, Y., Wu, Q., and Guan, J. (2013). Self-propelled micromotors driven by the magnesium–water reaction and their hemolytic properties. Angew. Chem., Int. Ed. Engl. *52*, 7208–7212. https://doi.org/10.1002/anie.201300913.
19. Li, T., Li, J., Morozov, K.I., Wu, Z., Xu, T., Rozen, I., Leshansky, A.M., Li, L., and Wang, J. (2017). Highly efficient freestyle magnetic nanoswimmer. Nano Lett. *17*, 5092–5098. https://doi.org/10.1021/acs.nanolett.7b02383.
20. Yu, J., Wang, B., Du, X., Wang, Q., and Zhang, L. (2018). Ultra-extensible ribbon-like magnetic microswarm. Nat. Commun. *9*, 3260. https://doi.org/10.1038/s41467-018-05749-6.
21. Yigit, B., Alapan, Y., and Sitti, M. (2019). Programmable collective behavior in dynamically self-assembled mobile microrobotic swarms. Adv. Sci. *6*, 1801837. https://doi.org/10.1002/advs.201801837.
22. Wu, Z., Li, L., Yang, Y., Hu, P., Li, Y., Yang, S.Y., Wang, L.V., and Gao, W. (2019). A microrobotic system guided by photoacoustic computed tomography for targeted navigation in intestines in vivo. Sci. Robot. *4*, eaax0613. https://doi.org/10.1126/scirobotics.aax0613.
23. Tay, Z.W., Chandrasekharan, P., Chiu-Lam, A., Hensley, D.W., Dhavalikar, R., Zhou, X.Y., Yu, E.Y., Goodwill, P.W., Zheng, B., Rinaldi, C., and Conolly, S.M. (2018). Magnetic particle imaging-guided heating in vivo using gradient fields for arbitrary localization of magnetic hyperthermia therapy. ACS Nano *12*, 3699–3713. https://doi.org/10.1021/acsnano.8b00893.
24. Pokki, J., Ergeneman, O., Chatzipirpiridis, G., Lühmann, T., Sort, J., Pellicer, E., Pot, S.A., Spiess, B.M., Pané, S., and Nelson, B.J. (2017). Protective coatings for intraocular wirelessly controlled microrobots for implantation: Corrosion, cell culture, and in vivo animal tests. J. Biomed. Mater. Res. B Appl. Biomater. *105*, 836–845. https://doi.org/10.1002/jbm.b.33618.
25. Shields, C.W., and Velev, O.D. (2017). The evolution of active particles: Toward externally powered self-propelling and self-reconfiguring particle systems. Chem *3*, 539–559. https://doi.org/10.1016/j.chempr.2017.09.006.
26. Yánez-Sedeño, P., Campuzano, S., and Pingarrón, J. (2017). Janus particles for (bio) sensing. Appl. Mater. Today *9*, 276–288. https://doi.org/10.1016/j.apmt.2017.08.004.
27. Bente, K., Codutti, A., Bachmann, F., and Faivre, D. (2018). Biohybrid and bioinspired magnetic microswimmers. Small *14*, 1704374. https://doi.org/10.1002/smll.201704374.
28. Ricotti, L., Trimmer, B., Feinberg, A.W., Raman, R., Parker, K.K., Bashir, R., Sitti, M., Martel, S., Dario, P., and Menciassi, A. (2017). Biohybrid actuators for robotics: A review of devices actuated by living cells. Sci. Robot. *2*, eaaq0495. https://doi.org/10.1126/scirobotics.aaq0495.
29. Ji, F., Li, T., Yu, S., Wu, Z., and Zhang, L. (2021). Propulsion gait analysis and fluidic trapping of swinging flexible nanomotors. ACS Nano *15*, 5118–5128. https://doi.org/10.1021/acsnano.0c10269.

30. Cui, J., Huang, T.Y., Luo, Z., Testa, P., Gu, H., Chen, X.Z., Nelson, B.J., and Heyderman, L.J. (2019). Nanomagnetic encoding of shape-morphing micromachines. Nature *575*, 164–168. https://doi.org/10.1038/s41586-019-1713-2.

31. Lee, S., Kim, J.Y., Kim, J., Hoshiar, A.K., Park, J., Lee, S., Kim, J., Pané, S., Nelson, B.J., and Choi, H. (2020). A needle-type microrobot for targeted drug delivery by affixing to a microtissue. Adv. Healthcare Mater. *9*, 1901697. https://doi.org/10.1002/adhm.201901697.

32. Wang, W., and Zhou, C. (2021). A journey of nanomotors for targeted cancer therapy: Principles, challenges, and a critical review of the state-of-the-art. Adv. Healthcare Mater. *10*, 2001236. https://doi.org/10.1002/adhm.202001236.

33. Venugopalan, P.L., Esteban-Fernández de Ávila, B., Pal, M., Ghosh, A., and Wang, J. (2020). Fantastic voyage of nanomotors into the cell. ACS Nano *14*, 9423–9439. https://doi.org/10.1021/acsnano.0c05217.

34. Park, S., and Yossifon, G. (2020). Micromotor-based biosensing using directed transport of functionalized beads. ACS Sens. *5*, 936–942. https://doi.org/10.1021/acssensors.9b02041.

35. Li, T., Zhang, A., Shao, G., Wei, M., Guo, B., Zhang, G., Li, L., and Wang, W. (2018). Janus microdimer surface walkers propelled by oscillating magnetic fields. Adv. Funct. Mater. *28*, 1706066. https://doi.org/10.1002/adfm.201706066.

36. Johnson, J.N., Nourhani, A., Peralta, R., McDonald, C., Thiesing, B., Mann, C.J., Lammert, P.E., and Gibbs, J.G. (2017). Dynamic stabilization of Janus sphere trans-dimers. Phys. Rev. E *95*, 042609. https://doi.org/10.1103/PhysRevE.95.042609.

37. Hatch, H.W., Yang, S.Y., Mittal, J., and Shen, V.K. (2016). Self-assembly of trimer colloids: effect of shape and interaction range. Soft Matter *12*, 4170–4179. https://doi.org/10.1039/C6SM00473C.

38. Sacanna, S., Rossi, L., and Pine, D.J. (2012). Magnetic click colloidal assembly. J. Am. Chem. Soc. *134*, 6112–6115. https://doi.org/10.1021/ja301344n.

39. Barz, B., and Urbanc, B. (2014). Minimal model of self-assembly: Emergence of diversity and complexity. J. Phys. Chem. B *118*, 3761–3770. https://doi.org/10.1021/jp412819j.

40. Jang, B., Hong, A., Alcantara, C., Chatzipirpiridis, G., Martí, X., Pellicer, E., Sort, J., Harduf, Y., Or, Y., Nelson, B.J., and Pané, S. (2019). Programmable locomotion mechanisms of nanowires with semihard magnetic properties near a surface boundary. ACS Appl. Mater. Interfaces *11*, 3214–3223. https://doi.org/10.1021/acsami.8b16907.

41. Hu, W., Lum, G.Z., Mastrangeli, M., and Sitti, M. (2018). Small-scale soft-bodied robot with multimodal locomotion. Nature *554*, 81–85. https://doi.org/10.1038/nature25443.

42. Martinez-Pedrero, F., Navarro-Argemí, E., Ortiz-Ambriz, A., Pagonabarraga, I., and Tierno, P. (2018). Emergent hydrodynamic bound states between magnetically powered micropropellers. Sci. Adv. *4*, eaap9379. https://doi.org/10.1126/sciadv.aap9379.

43. Lin, Z., Fan, X., Sun, M., Gao, C., He, Q., and Xie, H. (2018). Magnetically actuated peanut colloid motors for cell manipulation and patterning. ACS Nano *12*, 2539–2545. https://doi.org/10.1021/acsnano.7b08344.

44. Xie, H., Sun, M., Fan, X., Lin, Z., Chen, W., Wang, L., Dong, L., and He, Q. (2019). Reconfigurable magnetic microrobot swarm: Multimode transformation, locomotion, and manipulation. Sci. Robot. *4*, eaav8006. https://doi.org/10.1126/scirobotics.aav8006.

45. Gong, D., Cai, J., Celi, N., Liu, C., Zhang, W., Feng, L., and Zhang, D. (2019). Controlled propulsion of wheel-shape flaky microswimmers under rotating magnetic fields. Appl. Phys. Lett. *114*, 123701. https://doi.org/10.1063/1.5090297.

46. Gao, W., Pei, A., Feng, X., Hennessy, C., and Wang, J. (2013). Organized self-assembly of janus micromotors with hydrophobic hemispheres. J. Am. Chem. Soc. *135*, 998–1001. https://doi.org/10.1021/ja311455k.

47. Mou, F., Pan, D., Chen, C., Gao, Y., Xu, L., and Guan, J. (2015). Magnetically modulated pot-like MnFe2O4 micromotors: Nanoparticle assembly fabrication and their capability for direct oil removal. Adv. Funct. Mater. *25*, 6173–6181. https://doi.org/10.1002/adfm.201502835.

48. Gao, Y., Mou, F., Feng, Y., Che, S., Li, W., Xu, L., and Guan, J. (2017). Dynamic colloidal molecules maneuvered by light-controlled janus micromotors. ACS Appl. Mater. Interfaces *9*, 22704–22712. https://doi.org/10.1021/acsami.7b05794.

49. Wang, W., Duan, W., Sen, A., and Mallouk, T.E. (2013). Catalytically powered dynamic assembly of rod-shaped nanomotors and passive tracer particles. Proc. Natl. Acad. Sci. USA *110*, 17744–17749. https://doi.org/10.1073/pnas.1311543110.

50. Yu, S., Ma, N., Yu, H., Sun, H., Chang, X., Wu, Z., Deng, J., Zhao, S., Wang, W., Zhang, G., et al. (2019). Self-propelled Janus microdimer swimmers under a rotating magnetic field. Nanomaterials *9*, 1672. https://doi.org/10.3390/nano9121672.

51. Bozuyuk, U., Alapan, Y., Aghakhani, A., Yunusa, M., and Sitti, M. (2021). Shape anisotropy-governed locomotion of surface microrollers on vessel-like microtopographies against physiological flows. Proc. Natl. Acad. Sci. USA *118*, e2022090118. https://doi.org/10.1073/pnas.2022090118.

52. Yu, S., Li, T., Ji, F., Zhao, S., Liu, K., Zhang, Z., Zhang, W., and Mei, Y. (2022). Trimer-like microrobots with multimodal locomotion and reconfigurable capabilities. Mater. Today Adv. *14*, 100231. https://doi.org/10.1016/j.mtadv.2022.100231.

53. Yang, T., Tomaka, A., Tasci, T.O., Neeves, K.B., Wu, N., and Marr, D.W.M. (2019). Microwheels on microroads: Enhanced translation on topographic surfaces. Sci. Robot. *4*, eaaw9525. https://doi.org/10.1126/scirobotics.aaw9525.

54. Tasci, T.O., Herson, P.S., Neeves, K.B., and Marr, D.W.M. (2016). Surface-enabled propulsion and control of colloidal microwheels. Nat. Commun. *7*, 10225. https://doi.org/10.1038/ncomms10225.

55. Nishiguchi, D., Iwasawa, J., Jiang, H.R., and Sano, M. (2018). Flagellar dynamics of chains of active Janus particles fueled by an AC electric field. New J. Phys. *20*, 015002. https://doi.org/10.1088/1367-2630/aa9b48.

56. Yang, T., Tasci, T.O., Neeves, K.B., Wu, N., and Marr, D.W.M. (2017). Magnetic microlassos for reversible cargo capture, transport, and release. Langmuir *33*, 5932–5937. https://doi.org/10.1021/acs.langmuir.7b00357.

57. Martinez-Pedrero, F., and Tierno, P. (2015). Magnetic propulsion of self-assembled colloidal carpets: Efficient cargo transport via a conveyor-belt effect. Phys. Rev. Appl. *3*, 051003. https://doi.org/10.1103/PhysRevApplied.3.051003.

58. Yu, S., Sun, Z., Zhang, Z., Sun, H., Liu, L., Wang, W., Li, M., Zhao, Q., and Li, T. (2021). Magnetic microdimer as mobile meter for measuring plasma glucose and lipids. Front. Bioeng. Biotechnol. *9*, 779632. https://doi.org/10.3389/fbioe.2021.779632.

59. Nourhani, A., Brown, D., Pletzer, N., and Gibbs, J.G. (2017). Engineering contactless particle–particle interactions in active microswimmers. Adv. Mater. *29*, 1703910. https://doi.org/10.1002/adma.201703910.

60. Tierno, P., Golestanian, R., Pagonabarraga, I., and Sagués, F. (2008). Controlled swimming in confined fluids of magnetically actuated colloidal rotors. Phys. Rev. Lett. *101*, 218304. https://doi.org/10.1103/PhysRevLett.101.218304.

61. Yan, J., Bloom, M., Bae, S.C., Luijten, E., and Granick, S. (2012). Linking synchronization to self-assembly using magnetic Janus colloids. Nature *491*, 578–581. https://doi.org/10.1038/nature11619.

62. Mackay, F.E., Ollila, S.T.T., and Denniston, C. (2013). Hydrodynamic forces implemented into LAMMPS through a lattice-Boltzmann fluid. Comput. Phys. Commun. *184*, 2021–2031. https://doi.org/10.1016/j.cpc.2013.03.024.

63. Chen, S., and Doolen, G.D. (1998). Lattice boltzmann method for fluid flows. Annu. Rev. Fluid Mech. *30*, 329–364. https://doi.org/10.1146/annurev.fluid.30.1.329.

64. Ye, H., Shen, Z., and Li, Y. (2018). Computational modeling of magnetic particle margination within blood flow through LAMMPS. Comput. Mech. *62*, 457–476. https://doi.org/10.1007/s00466-017-1508-y.

STAR★METHODS

KEY RESOURCES TABLE

REAGENT or RESOURCE	SOURCE	IDENTIFIER
Chemicals, peptides, and recombinant proteins		
SiO_2 microspheres	Macklin	7631-86-9
Alginate	Macklin	9005-38-3
$CaCl_2$	Macklin	10043-52-4
Software and algorithms		
ImageJ	National Institutes of Health	https://imagej.net/ij/
Lammps	Sandia	https://www.lammps.org/
COMSOL Multiphysics	COMSOL	https://www.comsol.com/
Other		
Turbomolecular pumped coater	Quorum	Q150T Plus
Data acquisition	National Instruments	NI-PCI-6259
Inverted optical microscope	Olympus	IX73

RESOURCE AVAILABILITY

Lead contact

Further information and requests for resources and materials should be directed to and will be fulfilled by the lead contact, Prof. Tianlong Li (tianlongli@hit.edu.cn).

Materials availability

This study did not generate new unique reagents.

Data and code availability

- Data reported in this paper will be shared by the lead contact upon request.
- This paper does not report original code.
- Any additional information required to reanalyze the data reported in this paper is available from the lead contact upon request.

METHOD DETAILS

Fabrication of the magnetic drug-carrying sphere

Magnetic Janus microspheres were obtained by depositing a layer of Ni on SiO_2 microspheres (5, 8, and 10 μm). Specifically, silica microspheres were with deionized (DI) water and then attached onto the surface of a glass slide. Then a turbomolecular pumped coater (Q150T Plus, Quorum, England) was used to deposit a 100 nm thick Ni layer and a 100 nm thick Au layer on SiO_2 microspheres. Next, the Janus microspheres attached on the glass were magnetized in different directions using a magnetizer at 2.5 T. After the deposition, a mixture containing alginate (2%, w/v) and DOX was dropped on the glass slide and then dried with N_2 gas. Aqueous $CaCl_2$ (0.2 mL of 5%, w/v) was then dropped onto the glass slide to cross-link alginate. After 30 min, the glass slides were washed with pure water and dried with N_2 gas. After a brief sonication in ultrapure water, the Janus microspheres were released from the glass slide and dispersed into ultrapure water before use.

Magnetic actuation system

All magnetic drive motion experiments were conducted in the external magnetic field generator shown in Figure S4, which was composed of coil group, data acquisition, power amplifier and PC terminal. Three degrees of freedom Helmholtz coils arranged on a microscope realize the driving and observation of the microrobot. When driving microrobots, the LabVIEW program in the PC controlled a high-speed data acquisition (DAQ NI-PCI-6259) card to generate a driving signal, which was amplified by voltage amplifiers to drive the coils to generate a uniform rotating magnetic field in any plane in the 3D space. The parameters of the coil and the corresponding relationship between the internal current and the generated magnetic field are listed in Table S1. Motion behaviors of microrobots were captured at 25 frame·s^{-1} by an inverted optical microscope (IX73, Olympus, Tokyo, Japan).

Environmental details of experiments

The basic exploration of the multimodal motion rules of microdimer robots was carried out in a water environment, and the analysis was carried out for both configurations of microdimer robots. For application research on biological surface topography and *ex vivo* environments, the HTH configuration microdimer robot with better movement performance was selected. The environmental details of experiments and simulation are shown in Table 1.

Simulation analysis

The simulations were performed within the framework of COMSOL Multiphysics 5.5 and large-scale atomic/molecular massively parallel simulator (LAMMPS). Computational fluid dynamics (CFD) simulations were performed in a 3D plane by solving the Navier–Stokes equations for microdimer robots placed in a rectangular microfluidic channel filled with deionized water as media. The top and bottom surfaces of the channel were defined as no-slip boundaries, and the distance between the microdimer robot and the bottom surface was 200 nm.

In the molecular dynamic simulation, Lattice Boltzmann (LB) method and originally implemented solver of *fix_lb_fluid* were used to solve Navier–Stokes equations.[61–64] Each Janus microsphere was regarded as a sphere with a point dipole shifted from the geometric center of sphere. The magnetic interactions of the different microspheres are calculated at each time step by solving a linear system of equations for the magnetic moment of each microsphere, which results from the synergy of the magnetic and fluid fields. The movement of a magnetic Janus microsphere was obtained by solving Newton's second law equation integrating with a Leapfrog algorithm. In the simulations, the Janus particles are modeled as paramagnetic spheres with anisotropic magnetic susceptibility, of which the dipole moment is shifted from the geometric center, the same used by Yan et al.[1]. The particle diameters are equivalent to the physical diameter of 5 μm and 8 μm, and the particle density is taken to be 2.5 g/m^3. The fluid viscosity is taken to be 1.0 mPa s corresponding approximately to the viscosity of water at room temperature.

At each time step (1 × 10^{-7} s), magnetic interactions are re-evaluated by solving the linear system of equations for each particle's magnetic moment as a function of the field produced by the other particles and the spatially uniform, time-dependent external field. For each of the n particles, there is an equation for the magnetic moment $\vec{m}_i$,

$$\vec{m}_i = \chi \vec{H}_{total} = \chi\left(\vec{H}_{j\neq i} + \vec{H}\right) \quad \text{(Equation 4)}$$

where χ is the anisotropic magnetic susceptibility tensor ($\chi_\perp$ = 21.870 and $\Delta\chi$ = 10.619), and $\vec{H}_{j\neq i}$ is the magnetic field produced by all other particles, which is a linear function of the magnetic moments $\vec{m}_j$ for $j \neq i$.

As the magnetic particles will experience magnetic force in the fluid flow due to the external magnetic field and dipole–dipole interaction, the movement of these particles are driven by the force, not the velocity of the fluid flow. Meanwhile, the particles will experience a drag force due to the difference of velocity between these particles and surrounding fluid [2]. The fluid drag force $\mathbf{F}_f$ can be calculated using Stokes' approximation for a spherical particle in laminar flow [3]:

$$\mathbf{F}_f = C_d(\mathbf{u}_i - \mathbf{u}_f) \quad \text{(Equation 5)}$$

where $\mathbf{u}_i$ is the translational velocity of the magnetic Janus particles, $\mathbf{u}_f$ is the fluid velocity at the same place of the Janus particles. Here, $C_d = 6\pi\mu a$ is the drag coefficient, where a is the radius of the Janus particles. Then the governing equation for the motion of magnetic Janus particles under influence of external magnetic field and fluid field can be expressed by:

$$m_i\frac{d\mathbf{u}_i}{dt} = \mathbf{F}_f + \mathbf{F}_d \quad \text{(Equation 6)}$$

$$I_i\frac{d\omega_i}{dt} = \mathbf{T}_m + \mathbf{T}_d \quad \text{(Equation 7)}$$

where m_i and I_i is the mass and moment of inertia of the magnetic particle, $\mathbf{u}_i$ and ω_i are the translational and angular velocities of particle i, $\mathbf{F}_f$ are the fluid drag force, $\mathbf{F}_d$ and $\mathbf{T}_d$ is the summation of forces due to magnetic and repulsive interactions between particles, $\mathbf{T}_m$ is the torque due to external magnetic field.

To reflect the finite size effect of Janus microspheres, steric repulsion interactions between two magnetic particles are also considered. The force is approximated by the shifted-truncated Lennard Jones (STLJ) potential [4]. The purely-repulsive potential function $U_0(r)$ is provided by:

$$U_0(r) = \begin{cases} 4\varepsilon\left[\left(\frac{\sigma}{r}\right)^{12} - \left(\frac{\sigma}{r}\right)^{6}\right] + \varepsilon, r < r_0 \\ 0, r \geq r_0 \end{cases} \quad \text{(Equation 8)}$$

where the parameters r, ε and σ represent the distance between microsphere centers, potential well depth and equilibrant distance, respectively. With a value of $2^{1/6}\sigma$, $r0$ corresponds to the minimum of Lennard-Jones potential.

QUANTIFICATION AND STATISTICAL ANALYSIS

All data were shown as means ± SD via at least triplicate samples. A two-tailed, Student's *t* test was used for testing the significance between two groups. A one-way analysis of variance (ANOVA) with Dunnett's test was performed to test the significance for multiple comparisons. A statistical significance was assumed at $p < 0.05$. Samples were randomly allocated to different experimental groups.